Received: 20 May 2022 | Revised: 12 December 2022 | Accepted: 12 December 2022

DOI: 10.1002/mp.16185

RESEARCH ARTICLE

MEDICAL PHYSICS

Deep learning for x-ray scatter correction in dedicated breast CT

Juan J. Pautasso[1] | **Marco Caballo**[1] | **Mikhail Mikerov**[1] | **John M. Boone**[2,3] | **Koen Michielsen**[1] | **Ioannis Sechopoulos**[1,4,5]

[1]Department of Medical Imaging, Radboud University Medical Center, Nijmegen, The Netherlands

[2]Department of Radiology, University of California Davis, Sacramento, California, USA

[3]Department of Biomedical Engineering, University of California Davis, Sacramento, California, USA

[4]Dutch Expert Centre for Screening (LRCB), Nijmegen, The Netherlands

[5]Technical Medical Centre, University of Twente, Enschede, The Netherlands

Correspondence
Ioannis Sechopoulos, Radboud University Medical Center, Postbus 9101, 6500 HB, Nijmegen (766), Geert Grooteplein 10 (route 767), Nijmegen, The Netherlands.
Email: Ioannis.Sechopoulos@radboudumc.nl

Funding information
European Research Council (ERC); European Union's Horizon 2020, Grant/Award Number: 864929

Background: Accurate correction of x-ray scatter in dedicated breast computed tomography (bCT) imaging may result in improved visual interpretation and is crucial to achieve quantitative accuracy during image reconstruction and analysis.
Purpose: To develop a deep learning (DL) model to correct for x-ray scatter in bCT projection images.
Methods: A total of 115 patient scans acquired with a bCT clinical system were segmented into the major breast tissue types (skin, adipose, and fibroglandular tissue). The resulting breast phantoms were divided into training (n = 110) and internal validation cohort (n = 5). Training phantoms were augmented by a factor of four by random translation of the breast in the image field of view. Using a previously validated Monte Carlo (MC) simulation algorithm, 12 primary and scatter bCT projection images with a 30-degree step were generated from each phantom. For each projection, the thickness map and breast location in the field of view were also calculated. A U-Net based DL model was developed to estimate the scatter signal based on the total input simulated image and trained single-projection-wise, with the thickness map and breast location provided as additional inputs. The model was internally validated using MC-simulated projections and tested using an external data set of 10 phantoms derived from images acquired with a different bCT system. For this purpose, the mean relative difference (MRD) and mean absolute error (MAE) were calculated. To test for accuracy in reconstructed images, a full bCT acquisition was mimicked with MC-simulations and then assessed by calculating the MAE and the structural similarity (SSIM). Subsequently, scatter was estimated and subtracted from the bCT scans of three patients to obtain the scatter-corrected image. The scatter-corrected projections were reconstructed and compared with the uncorrected reconstructions by evaluating the correction of the cupping artifact, increase in image contrast, and contrast-to-noise ratio (CNR).
Results: The mean MRD and MAE across all cases (min, max) for the internal validation set were 0.04% (−1.1%, 1.3%) and 2.94% (2.7%, 3.2%), while for the external test set they were −0.64% (−1.6%, 0.2%) and 2.84% (2.3%, 3.5%), respectively. For MC-simulated reconstruction slices, the computed SSIM was 0.99 and the MAE was 0.11% (range: 0%, 0.35%) with a single outlier slice of 2.06%. For the three patient bCT reconstructed images, the correction increased the contrast by a mean of 25% (range: 20%, 30%), and reduced the cupping artifact. The mean CNR increased by 0.32 after scatter correction, which was

not found to be significant (95% confidence interval: [−0.01, 0.65], $p = 0.059$). The time required to correct the scatter in a single bCT projection was 0.2 s on an NVIDIA GeForce GTX 1080 GPU.

Conclusion: The developed DL model could accurately estimate scatter in bCT projection images and could enhance contrast and correct for cupping artifact in reconstructed patient images without significantly affecting the CNR. The time required for correction would allow its use in daily clinical practice, and the reported accuracy will potentially allow quantitative reconstructions.

KEYWORDS
computed tomography, cone-beam breast CT, deep learning, Monte Carlo, scatter correction

1 | INTRODUCTION

When not addressed, x-ray scatter can be one of the main causes of degradation of image quality in x-ray imaging. For example, in tomographic imaging, it can be observed as a cupping artifact that affects the accuracy of the measured signal intensity. Its consequences are even more noticeable in cone beam computed tomography (CBCT), due to the large area of irradiation.[1–3] X-ray scatter not only results in a potentially suboptimal visual interpretation by radiologists, but also in quantitative inaccuracies that can affect image analysis.

Different methods have been proposed to correct the x-ray scatter signal in acquired images. In general, these can be divided into two groups: scatter suppression and scatter estimation.[4] In body CBCT, the former combines the use of an anti-scatter grid or collimation with software post-processing;[5–8] the latter consists of post-processing approaches that aim to estimate the scatter, and then correct the images by subtraction.[9–13]

The gold standard for scatter estimation is Monte Carlo simulation (MC).[2] However, although it can provide accurate estimates, its disadvantage lies in the time required to obtain such results, which hinders its application in clinical practice.[4] For this reason, to estimate the scatter in body CBCT images, algorithms based on DL trained with MC-simulated patient data have been developed.[4,14–17]

In breast imaging, dedicated breast computed tomography (bCT)[18–21] is not exempt from the effect of scatter.[22–24] In this modality, typically based on a CBCT system, the patient lies prone on a table with an opening through which the breast is placed. The x-ray tube and the detector are mounted on a rotating gantry, and a complete set of projections is obtained in a single revolution around the pendant breast. These projections are then reconstructed to obtain a 3D image capable of providing information about the anatomy of the breast and the presence of lesions, optionally with iodine contrast enhancement.[25–28]

As with body CBCT, several approaches have been proposed to avoid the undesirable effects of x-ray scatter in bCT. Most of them suppress the scatter signal by using anti-scatter grids or collimation, also combined with software postprocessing.[29–31] Moreover, solutions were also proposed in which specific hardware was developed and integrated into the bCT system to mitigate the effect of x-ray scatter.[32–34] Similarly, fully software-based solutions were also proposed to correct for scatter in bCT images.[35,36]

However, most previous methods developed to correct for the scatter signal in bCT either required the acquisition of an additional scan with an x-ray beam blocker (resulting in the need for additional hardware and yielding an increased dose and possibility of motion artifacts),[36] or they assumed the prior knowledge of breast shape and tissue composition, possibly leading to simplifications that may affect the accuracy of scatter estimation.[35]

Therefore, in this work, we propose and validate a software-based solution to estimate and correct the x-ray scatter present in bCT images. The developed method consists of a deep learning (DL) model for scatter estimation trained on MC-simulated primary and scatter bCT projections performed using patient-based breast phantoms. The method is devised to estimate the scatter directly from the input bCT projection image, which is then subtracted from the acquired projection, resulting in the desired correction.

2 | MATERIALS AND METHODS

2.1 | Patient-based phantom generation

A total of 115 previously-created patient-based phantoms[37,38] were used in this work. These were obtained from patient scans acquired with a clinical Koning breast CT (Koning Corp., Norcross, GA, USA) installed at Radboud University Medical Center, which were automatically segmented into the main tissues present in the breast: adipose tissue, fibroglandular tissue, and skin. The x-ray tube with a tungsten anode was set to 49 kV. An aluminum filter of 1.6 mm (1.39 mm Al 1st HVL) was used. Dose was set by the system automatic exposure control.

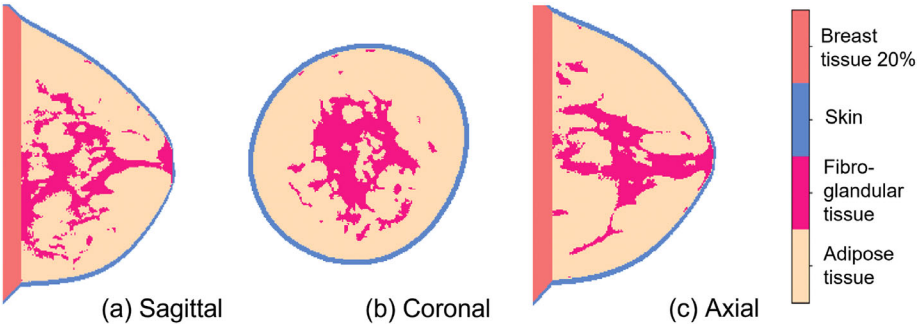

FIGURE 1 Example of a bCT patient-based phantom shown in the (a) sagittal, (b) coronal, and (c) axial views. Breast tissue 20% represents the 15 slices (4.1 mm) of added tissue near the chest wall, composed of a homogeneous mixture of 80% adipose and 20% fibroglandular tissue, by mass. This added tissue was inserted to compensate for the missing slices in the segmented breast CT phantoms, due to image artifacts in the region close to the chest wall

Due to the artifacts inherent to the modality that made the inclusion of information from the chest wall unfeasible during segmentation,[37] a total of 15 rows in which the pectoralis muscle was present had to be removed. However, a simplified version of the chest wall was added back during the MC simulations. To make sure that the phantom dimensions and location in the field of view matched the original patient scans, we compensated for this missing part by adding 15 slices (thickness per slice 0.273 mm) of homogeneous tissue, with each slice consisting of a dilation of the preceding slice. Since no information about the tissue type present in this region was available, this homogeneous breast tissue was modeled as a mixture of 80% adipose and 20% fibroglandular tissue, by mass. The added tissue ensures that the resulting scatter estimate from the MC simulations is correct, including any backscatter onto the detector from the patient's chest. This extrapolated region, unusable even uncorrected, was excluded when measuring performance. An example of a patient-based phantom is shown in Figure 1.

To increase the number of phantoms available to train and validate the developed DL model (described in Section 2.4), the initial number of patient-based phantoms was increased fourfold by random translation and then separated to devote for either training the model ($n = 440$ samples) or for validation ($n = 20$ samples). To achieve realistic augmentations, each phantom was translated up to 40 mm in a random direction along the coronal plane, to account for different possible breast positions in the field of view.

In addition, for independent testing, a set composed of another ten previously generated patient-based phantoms was collected. For this, ten patient scans acquired with a completely different bCT system named Doheny, developed and installed at the University of California, Davis, were retrieved.[21] The system was equipped with an x-ray tube was set at 60 kV. To filter the x-ray spectrum, a 0.2 mm copper filter (1.5 mm Al 1st HVL) was used.[20] A breast phantom was generated from each of these patient scans using the same method as that used for the first 115 phantoms.[37,38]

2.2 | Monte Carlo primary and scatter image simulation

The obtained samples were used to generate primary and scatter projection images using a previously-validated MC simulation algorithm based on the Geant4 toolkit (v10.07, December 2020).[39,40] All simulations were performed to replicate the geometry and acquisition settings of the clinical bCT system installed at Radboud University Medical Center. A 49 kV spectrum filtered with 1.6 mm Al was modeled[41] to match the 1st half value layer of 1.39 mm Al previously reported.[38] For each MC simulation, 2×10^8 x-rays were tracked. This number of primary histories results in an estimated maximum uncertainty lower than 10% in MC-simulated images, based on the uncertainty estimation method proposed by Sempau et al.[42]

During simulation, to recreate the geometry of the bCT system, a 397 mm × 248 mm bCT indirect flat panel detector was modeled as a 600 μm thick CsI scintillator layer and a pixel size of 3.104 mm to obtain images of 128 × 80 pixels in size.

The measured distance from the source to the detector was 923 mm, while the isocenter was located at 650 mm from the source. The type of x-ray field used was isotropic.

For each simulation, two outputs were obtained: the primary projection and the scatter projection, the latter involving the photons subjected to one or more interactions before reaching the detector. For each sample, a total of 12 simulations were performed, from 0° to 360° with a 30° step, to cover a complete gantry revolution.

Consequently, a total of 5460 primary and scatter projections of size 128 × 80 pixels were generated. To obtain the images representing the total x-ray energy absorbed in the detector, primary and scatter projections were summed.

2.3 | Data preprocessing and deep learning model inputs

All MC-simulated projection images were individually normalized to the 95th percentile of pixel intensity of the entire image. The DL model was trained single-projection-wise, that is, single total projection input, single scatter projection output, to maximize the ratio between ease of learning and computational efficiency.

However, only including 2D projection images as network input would result in the lack of any information in the third dimension, which can affect the scatter magnitude and distribution. To account for this, and still maintain a single projection-wise approach, two additional parameters were calculated for each MC simulated projection and provided as extra inputs to the model. The first was the breast location, for which the horizontal distance was calculated from the breast center of mass to the center of the projection image orthogonal to the view being processed. This input addresses the effect on the scatter distribution of the breast location along the direction orthogonal to the projection being processed. The second additional input was the breast thickness map associated with each projection image, which was obtained by reconstructing the acquired images and measuring the intersection length of the ray going from the source to each pixel of the imaged breast at the detector. This additional input provides information on the third dimension of the breast regarding its size and shape. To ease the training of the model for scatter estimation, the thickness maps were normalized to a similar range of pixel values as the original simulated projections, by applying the negative exponential thickness, as follows:

$$\text{normalized thickness map} = \exp\left(-\text{thickness map}/100\right) \quad (1)$$

Figure 2 shows an example for both additional inputs.

2.4 | Deep learning model architecture and training parameters

A U-Net-based[43] convolutional neural network (CNN) was developed as shown in Figure 3. The architecture consists of a contracting path and an equally-formed expansion path. In the contracting path, the number of feature channels was doubled at each downsampling step, with the input spatial dimensions being halved by using 2×2 max pooling layers. In the expansion path, the number of feature channels was doubled, as each step consists of a resampling of the feature map through 2×2 upsampling layers.

The total images were set as the main input at the first block of the contraction path, while the scatter projection images were given to the network as pixelwise labels for learning.

The output of each block from the contraction path was concatenated to the corresponding up-sampling block in the expansion path. The final layer was implemented with 1×1 convolutions to map the channels to the desired output.

For each convolutional layer of the network, padded 2D convolutions (padding = '*same*') with filter size 64, kernel size 3×3, and He Uniform initialization were implemented. Each convolution layer was followed by batch normalization (momentum = 0.99, epsilon = 0.001) and ReLU activation functions, except for the last layer. This layer consisted of a 2D convolutional filter with kernel size 1×1, and sigmoid activation. At the network bottleneck, both additional inputs (breast location and thickness map) were concatenated with the projection image features obtained from the contraction path. Specifically, the breast location was concatenated directly to the deepest network layer, as typically performed for the merging of scalar and convolutional features.[44]

The thickness map was concatenated at the same network depth, but, prior to concatenation, was further processed with an additional downsampling block, acting as a feature extractor.[43] The thickness map was concatenated at this location, instead of being given as a second channel to the original input (breast projection), to avoid replicating high-resolution features related to breast thickness from the contraction to the expansion path. Since information on breast thickness is useful only to provide extra three-dimensional information to the network, concatenating it in the network bottleneck (i.e., without replicating the thickness features between the encoder and the decoder) allows to maximize the training efficiency by making the learning of high-resolution features only from the input breast projection easier. Adam optimizer was used for training the model (batch size = 8, learning rate = 10^{-4}, 2000 epochs).

The loss function (L) consisted of a weighted mean squared error. For this, the square error was calculated by subtracting the ground truth MC-simulated image (y) from the DL-estimated scatter image ($\hat{y}$). The loss was weighted ten times more within the breast than in the open field. The breast area was identified in each projection by global thresholding. The equation L can be written as follows:

$$L = \frac{1}{n}\sum_{i=0}^{n}\left(10 * \left(y_{breast}^{(i)} - \hat{y}_{breast}^{(i)}\right)^2 + \left(y_{open\ field}^{(i)} - \hat{y}_{open\ field}^{(i)}\right)^2\right) \quad (2)$$

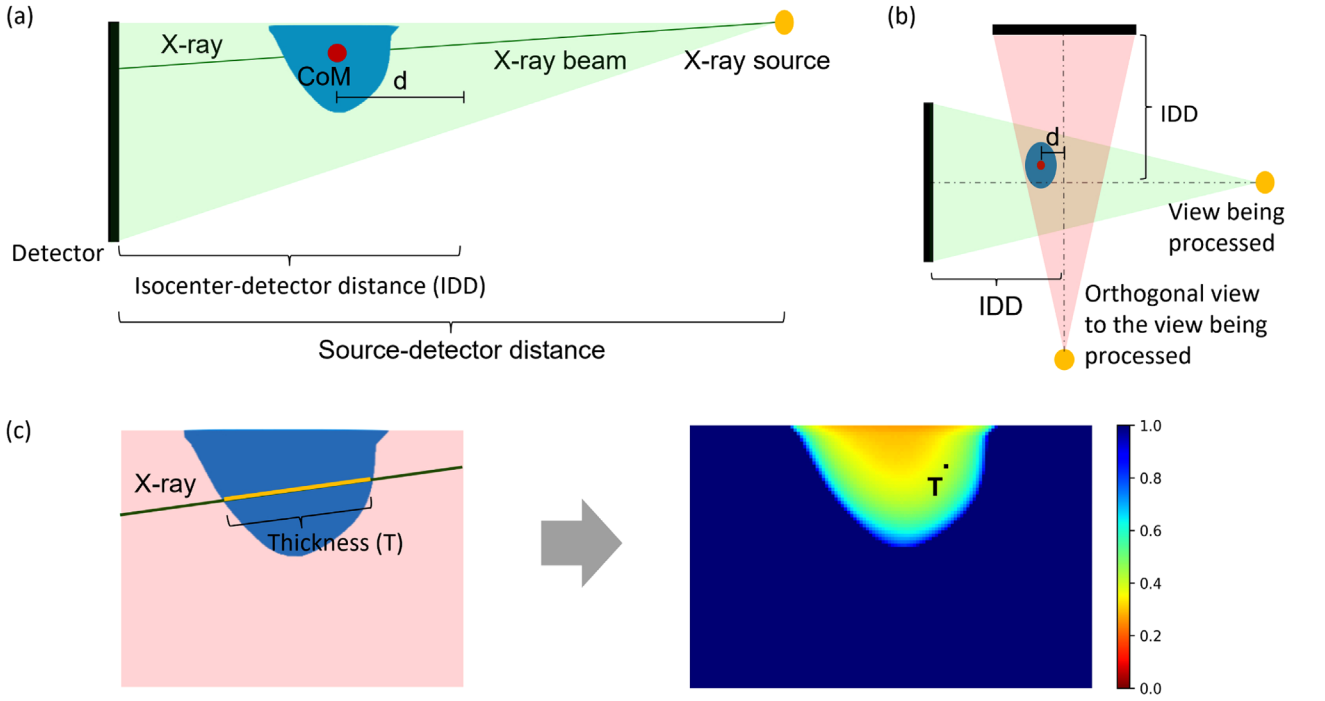

FIGURE 2 Example calculation of the two additional inputs: (a) shows a typical acquisition scenario where the source-detector and isocenter-detector distances are known. The center of mass (CoM) of the breast is at a distance d from the isocenter. The x-ray beam (light green) irradiating the breast and, as an example, a given x-ray beam (dark green line) are also shown. (b) shows how the horizontal distance from the center of mass of the breast to the center of the orthogonal projection image (x-ray beam in light red) is calculated. In addition, in (c), on the left, an example of the calculation of the intersection length of the beam from the source to one pixel of the imaged breast at the detector. The thicknesses obtained for each of the pixels of the breast imaged on the detector form the thickness map. Equation (1) is applied to normalize the map and the result is the image shown on the right

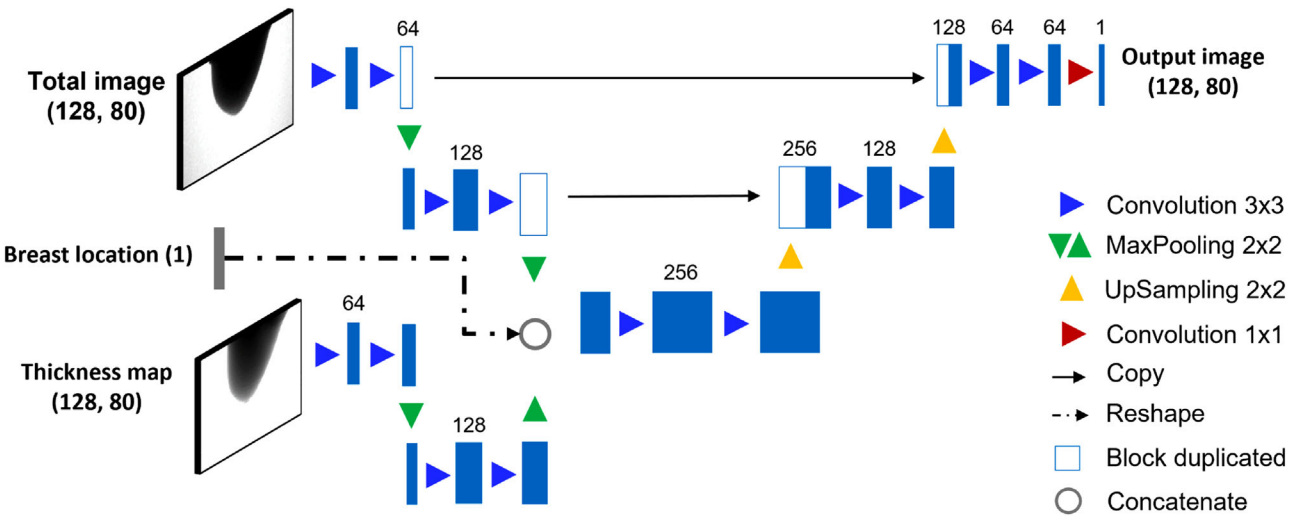

FIGURE 3 Schematic overview of the DL architecture used for scatter estimation. The total projection images of size 128 × 80 pixels were defined as the main input, while the respective thickness maps and the breast center of mass distance were included at the network bottleneck

2.5 | Deep learning model validation

DL-estimated scatter images were obtained from the MC-simulated total images of the validation ($n = 60$ projections from 5 breast samples) and test set ($n = 120$ projections from 10 breast samples), and then compared with the MC-simulated scatter images in the projection domain. Comparison was also performed by stratifying the validation and test set cases according to breast thickness, breast density (calculated, by mass, in the

original breast phantoms), and breast location, to evaluate the potential correlation of these factors on the scatter estimation error.

For model accuracy evaluation, the mean relative difference (MRD) and mean absolute error (MAE), both in percentages, were computed for all comparisons only considering the projected breast area (i.e., excluding the open field). The MAE in percentage was calculated as follows:

$$\mathrm{MAE}\,(\%) = \frac{100\%}{n}\sum_{i=1}^{n}\left|\frac{y_{i_{true_{MC}}} - y_{i_{estimated_{DL}}}}{y_{i_{true_{MC}}}}\right| \quad (3)$$

Where $y_{true_{MC}}$ and $y_{estimated_{DL}}$ are vectors containing all n pixels that conform the breast in the MC-simulated and the DL-estimated scatter images, respectively.

In a previous work[35] the effect of ignoring the chest wall was evaluated and found to have a negligible impact on the effectiveness of scatter correction (in addition to the fact that, as already mentioned, this part of the image is typically non-diagnostic due to image artifacts). Consequently, to calculate MRD and MAE in both sets (validation and test), the pixels of homogenous breast tissue (see Section 2.1) added at the chest wall in each projection were ignored.

2.5.1 | Effect of additional input parameters

Next, the benefit of the additional inputs (breast location and thickness map) was evaluated, by retraining the network with only the input MC projection, and with each of the extra inputs included. This comparison was performed retrospectively, that is, the architecture, hyperparameters, and training conditions were not modified. The error was calculated in each setting and plotted as a function of mean breast thickness.

2.5.2 | MC-simulated bCT acquisition

For a single phantom of the test set, MC simulations were repeated to generate 300 projections with an angular step of 1.2° (instead of a 30° step), to mimic a complete bCT acquisition. From this MC-simulated dataset, consisting of 300 primary (P_{MC}) and scatter (S_{MC}) projections, and their corresponding 300 total ($T_{MC} = P_{MC} + S_{MC}$) projections, three reconstructions were obtained and compared: the total uncorrected reconstruction using the T_{MC} projections, the primary-only reconstruction from the P_{MC} projections (or MC ground truth), and the corrected reconstruction from the T projections after DL-correction ($P' = T_{MC} - S_{DL}$). Image reconstruction was performed in all cases using a maximum likelihood in transmission method (ML-TR).[48] The structural similarity (SSIM) obtained with the "structural_similarity" function of the skimage metrics module (with sliding window size = 7) and the MAE between 100 slices (of the total ~500 slices) of the DL-corrected (P') and MC ground truth (P_{MC}) reconstructions were calculated.

2.6 | Application on clinical data

In addition to the tests performed on MC simulations, the scatter was corrected on three bCT patient images. These images were acquired with the bCT system installed at Radboud University Medical Center for an unrelated, ethics-approved trial.

To estimate the scatter present in these images, the bCT projections were resized to 128 × 80 and the model was applied. Then, the estimated scatter of the complete set was again resized to match the bCT acquisition dimensions. Finally, the estimated scatter was subtracted from the uncorrected images, and the results used for reconstruction.

To evaluate the reduction of the cupping artifact due to the scatter correction, visual and quantitative comparisons of the corrected and uncorrected bCT images were performed. For the former, 10 × 300 pixel profiles through specific axial slices were plotted. For the latter, ten ROIs of 20 × 20 pixels were placed on different regions of fibroglandular and adipose tissues in the reconstructed images, and the ROI mean values were measured and quantitatively compared. These ROIs were also used to calculate the local contrast as the difference of the measured fibroglandular and adipose divided by the adipose values, for both uncorrected and corrected images.

Furthermore, the obtained mean values from the different ROIs were compared to the theoretical linear x-ray attenuation values for adipose and fibroglandular tissues, to evaluate the recovery of voxel values compared to the theoretical attenuation values.[45–47] Linear attenuation coefficients were calculated for an x-ray energy of 27.8 keV, the average x-ray energy of the spectrum used for image acquisition. Reconstructed patient images were obtained by using ML-TR[48] with beam hardening correction to the mean energy of the spectrum.[49]

As a result, a range of x-ray linear attenuation values between 0.279–0.318 cm^{-1} and 0.385–0.416 cm^{-1} for adipose and fibroglandular tissues was used, considering the variability of x-ray attenuation properties reported for breast tissues across patients and publications.[45–47]

2.7 | Noise effect evaluation after scatter correction

After scatter correction by subtraction, an increase in the magnitude of high-frequency noise in the reconstructed

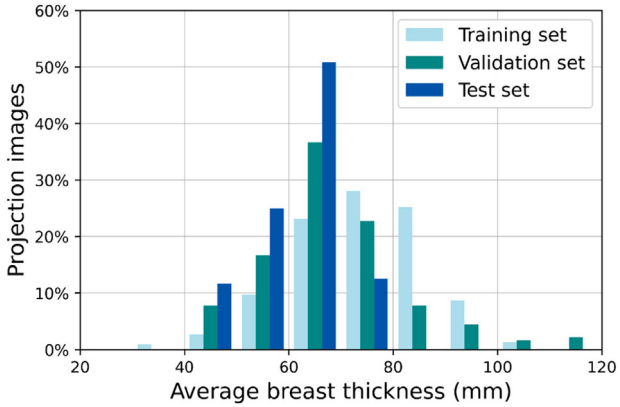

FIGURE 4 Histogram indicating average breast thickness distribution for the training (light blue), validation (dark cyan), and test (blue) sets. The number of projections in the training set (5280), validation set (60), and the test set (120) is expressed as a percentage with respect to the total number of cases in each dataset

CBCT images could be expected.[50] This could yield a reduction in the contrast-to-noise ratio (CNR) of the scatter-corrected image, which may negatively impact the benefit of scatter removal.[51] Therefore, the effect of noise after scatter correction was evaluated. For this, the ROIs for the local contrast calculation, described in the previous section, were used to calculate the CNR according to the following equation:

$$\mathrm{CNR} = \frac{\left|\bar{\mu}_{fibroglandular} - \bar{\mu}_{adipose}\right|}{\sqrt{\frac{\sigma^2_{figroglandular} + \sigma^2_{adipose}}{2}}} \quad (4)$$

Where $\bar{\mu}$ and σ^2 are the mean and variance, respectively, measured in each ROI. The CNR was calculated for the three uncorrected and DL-corrected bCT patient images, separately. To avoid the influence of the ROI location on the CNR calculation, the CNR was calculated between all 100 pairs of fibroglandular and adipose ROIs per bCT patient image. The CNR difference measured at the same ROI location pairs before and after correction was tested for significance using a mixed effects 2-way ANOVA with the scatter correction as fixed effect and the ROI locations as random effect.

3 | RESULTS

Figure 4 shows the distribution (in percentage) of the mean thicknesses of the breast samples that formed the training, validation, and tests sets, for all simulated projections.

In the training set, the model achieved a mean MRD and MAE between MC-simulated and DL-estimated scatter projections of 0.1% (range: −0.5%, 0.5%) and 3.1% (range: 2.5%, 3.4%), respectively. The calculated mean MRD and MAE across all cases for the validation set was 0.04% (range: −1.1%, 1.3%) and 2.94% (range: 2.7%, 3.2%), respectively. One sample in the validation set was found to have thickness along the direction of x-rays outside the range of 27—108 mm defined by the training set, as shown in Figure 4. Therefore, the mentioned sample was considered an outlier and excluded from the calculation of these average errors. For the test set, the MRD and MAE were −0.64% (range: −1.6%, 0.2%) and 2.84% (range: 2.3%, 3.5%), respectively. Individual errors on a projection level are shown in Figure 5, as a function of the mean breast thickness.

Figure 6 shows the MRD, in percentage, plotted as a function of breast density and of breast location, for the validation and test sets. The obtained Pearson's correlation coefficients calculated with the MRD as a function of breast location and breast density (by mass) were: 0.05, and −0.122 for the validation set; while for the test set, the computed values were: −0.217 and −0.190.

Figure 7 shows some example error maps between the MC-simulated and DL-estimated scatter projections obtained for two samples, one per bCT system (and therefore one for the internal validation, and one for the external test set). Error maps show the relative absolute percent error calculated pixelwise.

3.1 | Extra inputs effect

Figure 8 shows the effect of the two additional parameters used as input to the model on the validation and test performance. Numerical results are listed in Table 1.

3.2 | Monte Carlo simulated bCT acquisition

The SSIM computed over the evaluated set of 100 reconstructed slices was 0.99 and the MAE was 0.11% (range: 0%, 0.35%) with a single slice outlier of 2.06%. For that specific reconstructed slice where the outlier was found, the pixelwise difference between the reconstructed image of the ground truth and the estimated by DL was calculated, as shown in Figure 9.

In Figure 10, profiles were plotted for a single reconstruction slice from a full MC simulation 300 projection set.

3.3 | Application in clinical data

In Figure 11, profiles for a reconstructed slice of three different bCT patient acquisitions are shown. The model was found capable of accurately correcting the cupping artifact present in the uncorrected acquired images.

Figure 12 shows the box plots of the mean attenuation values for fibroglandular and adipose tissue, for

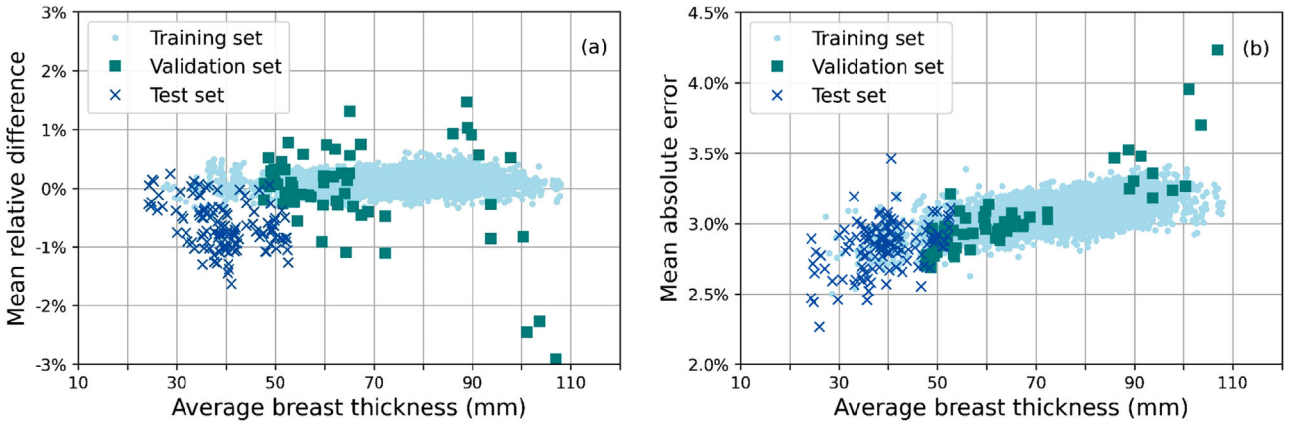

FIGURE 5 The (a) mean relative difference (MRD) and (b) mean absolute error (MAE), in percentage, between the MC-simulated and DL-estimated scatter images, as a function of breast thickness for each projection in the training, validation, and test set

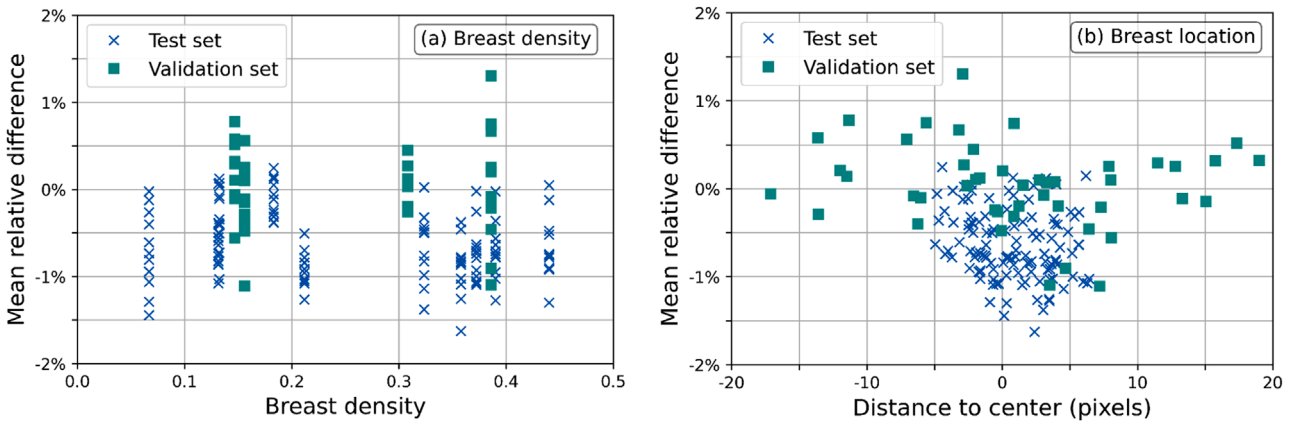

FIGURE 6 Mean relative difference (MRD), in percentage, between the MC-simulated and DL-estimated scatter images, plotted as a function of (a) breast density, and (b) breast location, to evaluate the effect of these factors on the scatter estimation error for the validation and test sets

TABLE 1 Achieved accuracy for each of the evaluated combinations: No extra inputs (None), only thickness maps as extra input, only breast location as extra input and then, both extra inputs (thickness maps and breast location). The calculated MRD and MAE (min, max) were listed for the validation and the test set

Extra inputs to the network			None	Thickness maps	Breast location	Both
Validation set	MRD	Mean	0.51%	−0.09%	0.96%	0.04%
		Min.	−1.84%	−1.69%	0.24%	−1.11%
		Max.	3.88%	2.00%	2.44%	1.30%
	MAE	Mean	3.19%	3.28%	3.03%	2.94%
		Min.	2.75%	2.89%	2.75%	2.69%
		Max.	4.45%	3.86%	3.52%	3.21%
Test set	MRD	Mean	−0.64%	−1.20%	−0.08%	−0.64%
		Min.	−3.35%	−2.93%	−0.92%	−1.63%
		Max.	1.86%	1.97%	0.87%	0.24%
	MAE	Mean	3.00%	3.86%	2.89%	2.84%
		Min.	2.27%	2.39%	2.36%	2.27%
		Max.	4.03%	5.01%	3.24%	3.46%

Abbreviations: MAE, mean absolute error; MRD, mean relative difference.

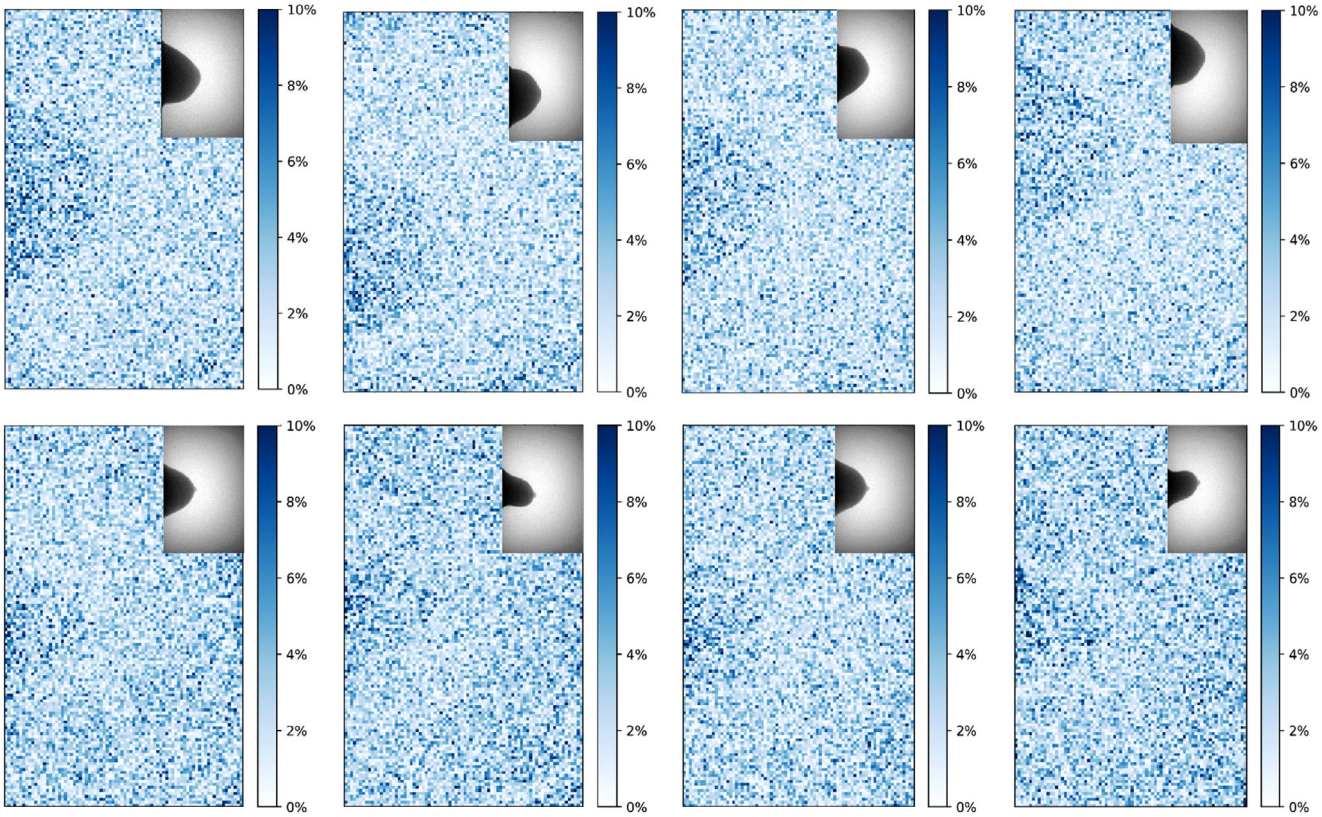

FIGURE 7 Example of error map between the MC-simulated and DL-estimated scatter images for two samples (in rows, one per acquisition system) at different acquisition angles (in columns, 0°, 90°, 180°, and 270°). Error maps show the relative absolute percent error (range: 0% to 10%) calculated pixelwise

the three evaluated patient cases, both uncorrected, and corrected with the developed DL model. As shown in the Figure, scatter correction could recover the average voxel values to the linear attenuation coefficient found in literature for both tissues.

The calculated contrast improvement for each patient case P1, P2, and P3 was 25%, 30%, and 20%, respectively. The mean CNR increased by 0.32 after scatter correction, which was not found to be significant (95% confidence interval: [−0.01, 0.65], $p = 0.059$). The residual distribution did not deviate from normal ($p = 0.84$). Figure 13 shows the box plots of the calculated CNRs for the three evaluated patient cases. The differences were found in both directions and are small, with the median values differing by less than 10%.

The time needed to correct the 300 projections of size 1024×640 pixels from a bCT scan is 58 s on a computer unit with an AMD Ryzen Threadripper 1950 × 16-Core Processor and NVIDIA GeForce GTX 1080 GPU. The calculated time involves each of the steps of the pipeline for obtaining the scatter-corrected image: normalization, calculation of thickness maps and of the horizontal distance, scatter estimation, inversion of the normalization to scale the intensity of the obtained scatter image to the input, and subtraction of the scatter image.

4 | DISCUSSION

In this work, we developed a DL model to estimate the x-ray scatter signal in bCT projection images. When evaluated against MC simulations, the model could achieve accurate results in projection domain. When evaluated in reconstruction domain, both on simulations and on patient data, the model could correct for the cupping artifacts due to the presence of scatter, could increase the image contrast, and could recover the voxel values to the expected linear attenuation coefficient.

The proposed model was devised to estimate the scatter from a single bCT projection, with three-dimensional image information learned through the two extra inputs provided (breast location in the orthogonal direction, and thickness map). When evaluating the effect of these two additional inputs on the model performance, the former achieved a further decrease in the dispersion of error values, and the latter helped avoid larger errors with increasing average breast thickness. These findings, therefore, confirmed the need for the inclusion of these two parameters for an optimized learning. In addition, they show that a single-projection-wise approach, when supplemented with these additional inputs, can yield accurate scatter estimates.

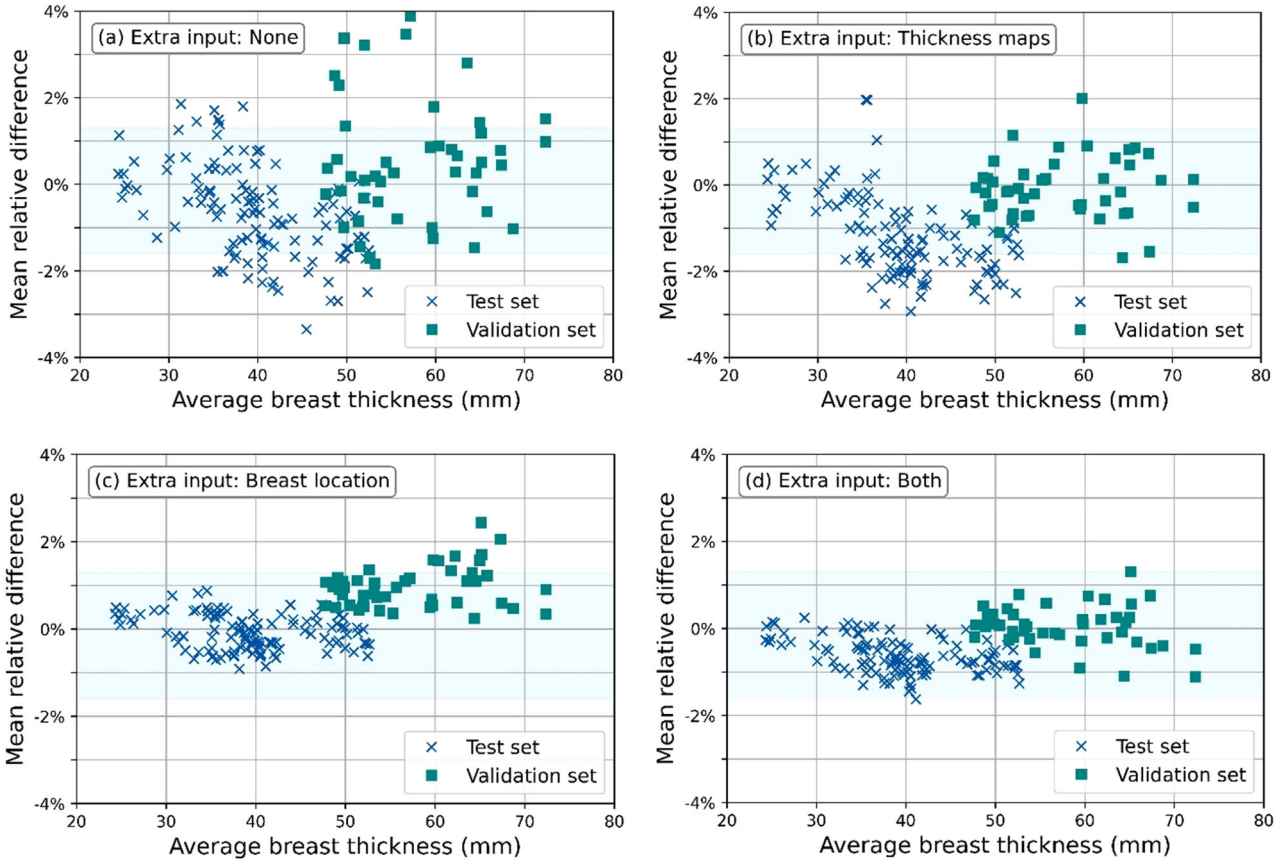

FIGURE 8 Mean relative difference (MRD) plotted as a function of average breast thickness from the validation and test set for the model trained: (a) without extra inputs, (b) with only the thickness maps added as extra input, (c) with only the breast location information added as extra input; and (d) with both the thickness maps and the breast location information added as extra inputs (equal to Figure 5a after removing outlier). The light blue band in each panel represents the range of values (min, max) of the data in panel (d)

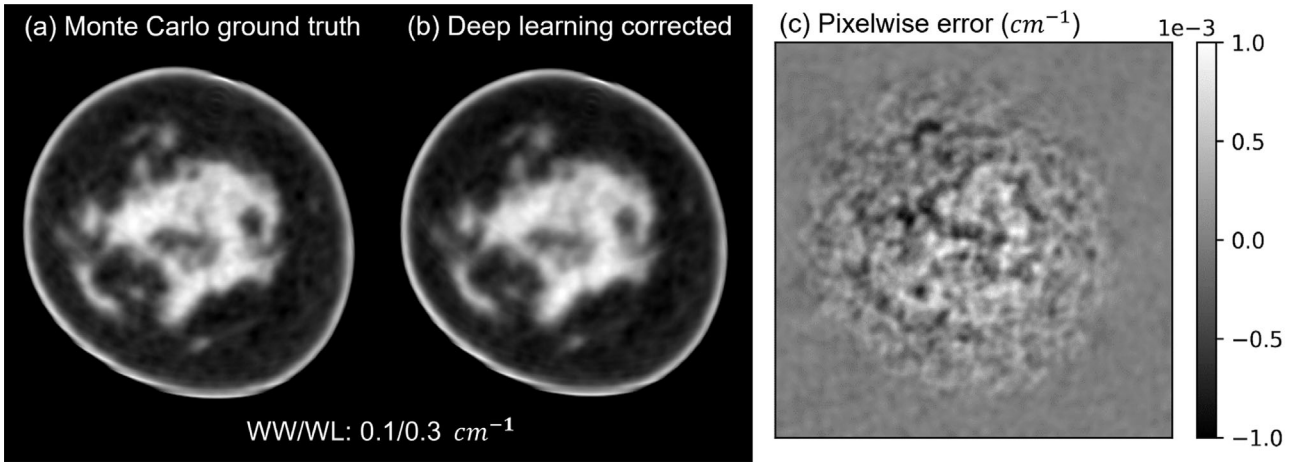

FIGURE 9 Reconstructed slice with outlier value: (a) Monte Carlo ground truth, (b) deep learning (DL) corrected, and (c) pixelwise error, in units cm^{-1}, obtained by subtracting both images

Moreover, because there is no useful information that can be analyzed from the reconstructed image due to the aforementioned artifacts, the chest wall was not taken into account in the error calculation. In any case, if the chest wall would have been removed completely, the resulting effect would have been minor, since Shi et al., showed that ignoring the chest wall has a negligible effect on the performance of scatter correction,

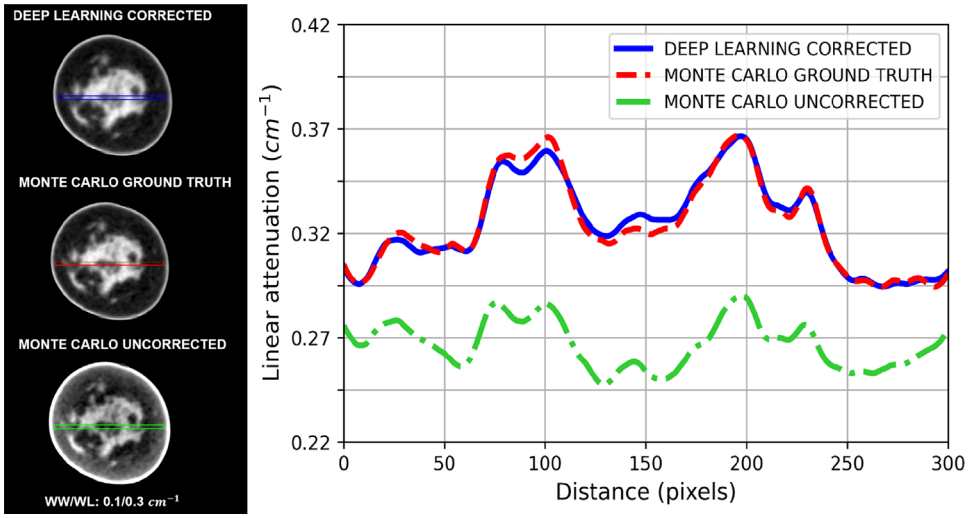

FIGURE 10 Example of profiles obtained for a Monte Carlo ground truth (red), deep-learning corrected (blue), and Monte Carlo uncorrected (green) for an MC-simulated reconstruction slice. Monte Carlo uncorrected refers to the total uncorrected reconstruction using the T_{MC} projections

mainly due to the strong signal attenuation in the chest wall region.[35]

The appropriateness of our DL approach seems to be also confirmed when put in perspective with previously reported findings obtained with DL models trained on MC simulations, performed mainly on body CBCT. For example, Maier et al., who presented a U-Net-based approach for scatter estimation in body CBCT[4] reported that, in fully reconstructed images, the calculated MAE between DL-estimated and MC-simulated scatter images for different anatomical regions was less than 1.8%. Furthermore, the time required for the estimation of scatter per projection was reported to be ≈0.01 s. In this work, when analyzing the error in the reconstructed images, the calculated MAE was less than 1%, while the time required to correct the scatter was ≈0.2 s per bCT projection. Of course, while this comparison is a further confirmation of our findings, direct comparison is not possible due to inherent differences in datasets and imaging systems.

MC based on GPU has been under research and development over a number of years,[52] often requiring simplification of some of the physical simulation processes. Although performing GPU-based MC simulations has resulted in orders of magnitude speedup, it appears that an MC-GPU approach would still require ∼10 h to correct a full scan of 300 bCT projections.[53]

Importantly, our results seem to indicate no relevant dependency of the estimated accuracy as a function of breast thickness, density, and location in the field of view. This suggests that a satisfactory scatter correction can be achieved even for large, very dense breasts, and even if the breast is not positioned precisely at the bCT isocenter during acquisition. Only a single exception was found (Figure 5), for which the estimation error (MAE) was found considerably higher (although still lower than 5%). However, this specific phantom presented an average breast thickness of 90 mm or higher in all simulated projections, being far from the training thickness distributions and being above the 90th percentile, according to previous literature.[55–57]

The profiles obtained from the DL-corrected patient bCT scans (Figure 11) showed a good agreement with the reported theoretical x-ray linear attenuation values for adipose and fibroglandular tissue in reconstructed bCT images. Furthermore, the correction could also achieve an increase in image contrast of 25%–35% compared to the uncorrected reconstructions. This increase in contrast was similar to that obtained in previous work aimed at scatter correction in bCT images, achieved through the acquisition of a second image with a perforated tungsten plate at the exit of the x-ray tube.[33] Therefore, our approach seems to yield state-of-the-art findings, but with the important advantage of not requiring any additional hardware components or the acquisition of any additional images.

In addition, no statistically significant difference in CNR values was found between the DL scatter-corrected and uncorrected reconstructions, the calculated CNR values are close to each other for all three cases and their differences vary in sign, indicating that the CNR in the images is not really affected by the scatter correction. Although relative noise increases when the estimated scatter is subtracted from the projection, contrast also increases, keeping the ratio between noise and contrast comparable and, therefore, accurate quantitative information can be obtained without compromising the detectability, at least as represented by CNR. The small contribution of the scatter image estimated by the developed DL method to the total noise

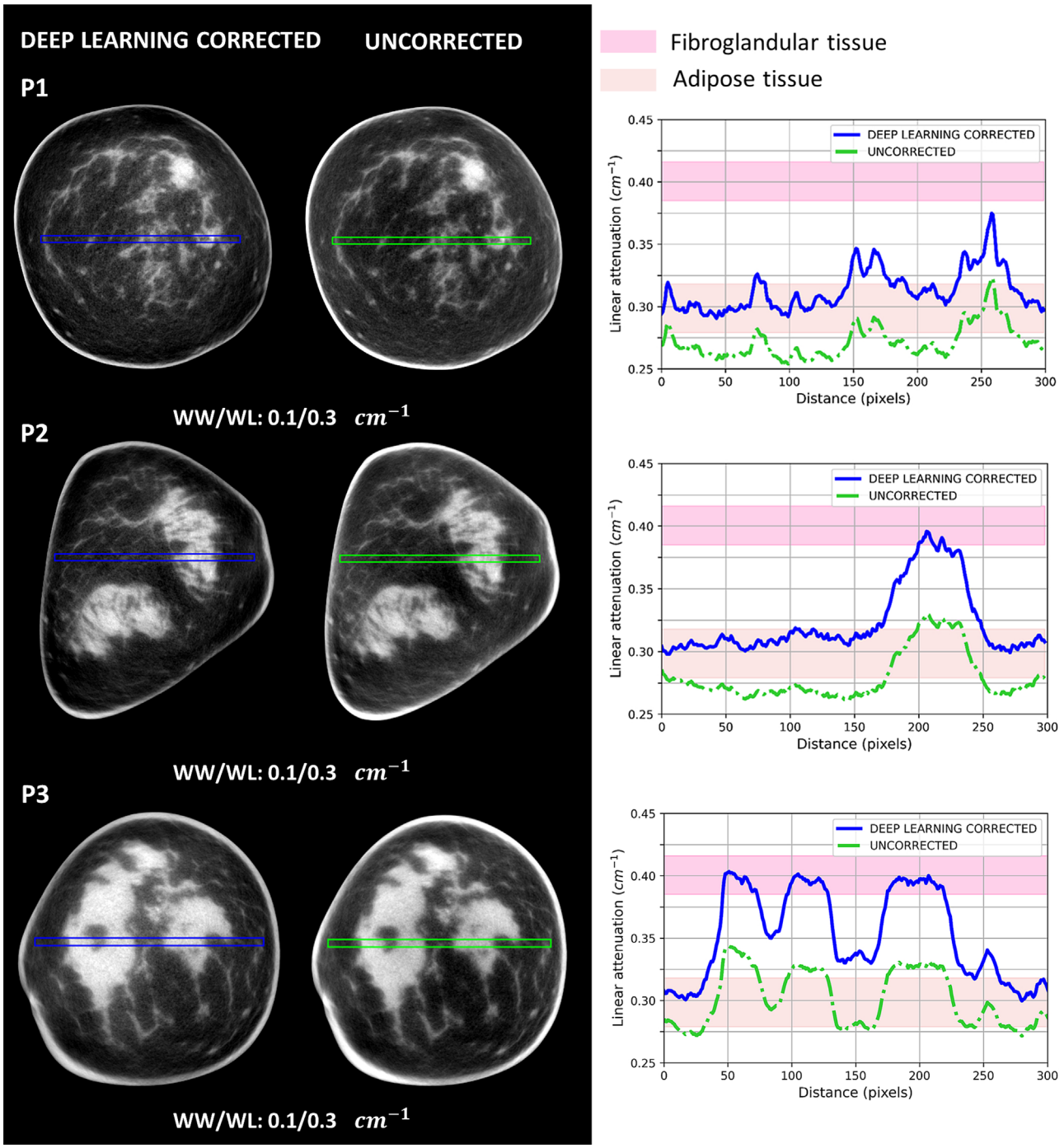

FIGURE 11 Example of profiles obtained for the three selected slices of reconstructed patient bCT images, both uncorrected and DL-corrected. The filled band represents the obtained range of x-ray linear attenuation values for fibroglandular (fuchsia) and adipose tissue (pink)

of the corrected image could be expected and may be attributable to the employed U-Net functioning as a denoiser in which many convolution layers help to generate noise-free or negligible noise output.[54]

In this study, we showed that the developed method can allow for quantitative image reconstruction, while it results in similar CNR values compared to uncorrected images. These factors point to the utility of the method in increasing image quality. However, although the CNR results are encouraging, they are not necessarily predictive of clinical task performance, which could be affected by other factors, such as higher noise correlations. In this work, we did not specifically test our approach for any clinical task, such as microcalcification detection

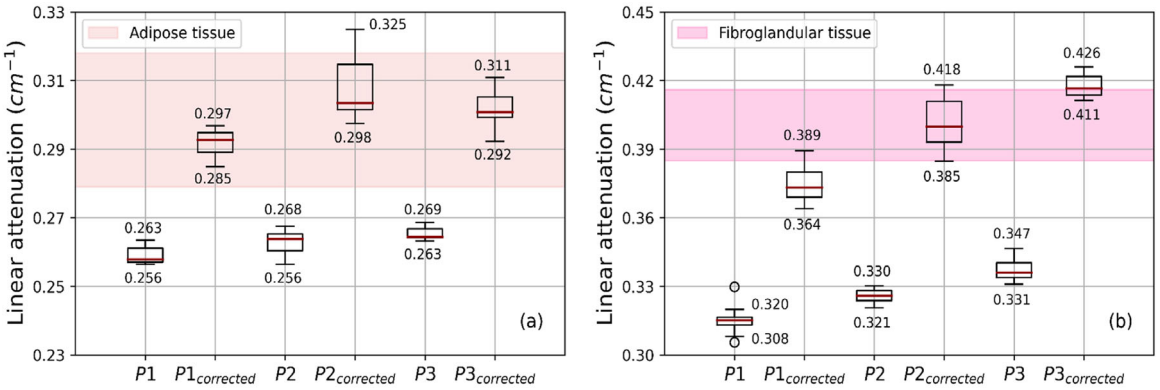

FIGURE 12 Boxplots showing the average voxel values for three reconstructed uncorrected and DL-corrected bCT patient images. The average voxel value was calculated in each patient image in 10 ROIs, half placed on adipose tissue (panel a) and half on fibroglandular tissue (panel b). The measured average thickness for each case was 74, 78, and 72 mm, respectively. The filled bands represent the range of x-ray linear attenuation values published for adipose (pink) and fibroglandular (fuchsia) tissues. The horizontal line inside the boxes (red) indicates the median while the upper and lower limits of the boxes represent the first and third quartiles. The whiskers represent the maximum and minimum values which are shown on the plot

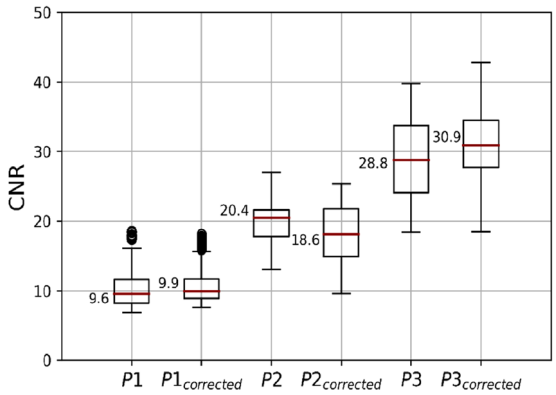

FIGURE 13 Boxplots showing the CNR values for the three example cases. The horizontal red line inside the boxes indicates the median, the boxes represent the first and third quartiles, and the whiskers represent the maximum and minimum values

performance. Of course, to further evaluate the appropriateness of our methods for patient image correction and clinical tasks, future work could include a larger image dataset and human or model observers for comprehensive validation of the developed method on clinical data.

A limitation of the developed work is the potential dependency of the accuracy in scatter prediction for very large breasts (although, as mentioned, this effect was relevant only for breast above the 90th percentiles[55–57]). For this reason, to enlarge the range of the population currently considered, larger samples will be included in our training set during future investigations.

As a second limitation, the model was developed considering only a single bCT acquisition setting. If the imaging conditions vary considerably, the model must be re-trained.

In our future research, we plan to use the developed model to correct the scatter in contrast-enhanced dynamic bCT.[28] Since this involves using multiple different exposure settings, we will extend our work to generalize to the different spectra in this new system. Thanks to scatter correction, accurate image reconstruction will be possible, allowing for the correct quantification of contrast-enhancement from breast tissues and lesions, a recognized biomarker of breast lesion malignancy and aggressiveness.

5 | CONCLUSION

We developed a DL model to estimate the x-ray scatter signal in bCT projection images. This model was able to estimate scatter with high accuracy, resulting in scatter-corrected images with improved contrast and without significantly affecting the CNR. These corrected images can therefore potentially be useful to improve diagnostic performance and, importantly, yield quantitative bCT image reconstructions where voxel values reflect the true physical properties of breast tissues. Furthermore, the short time required by the model to estimate (and correct) the x-ray scatter can allow its use in daily clinical practice.

ACKNOWLEDGMENTS

This project has received funding from the European Research Council (ERC) under the European Union's Horizon 2020 research and innovation programme (grant agreement No 864929).

CONFLICT OF INTEREST

The authors have no conflicts of interest directly relevant to this work to disclose.

REFERENCES

1. Niu T, Zhu L. Overview of x-ray scatter in cone-beam computed tomography and its correction methods. *Curr Med Imag Rev*. 2010;6(2):82-89. doi:10.2174/157340510791268515
2. Rührnschopf EP, Klingenbeck K. A general framework and review of scatter correction methods in x-ray cone-beam computerized tomography. Part 1: scatter compensation approaches [published correction appears in *Med Phys*. 2011;38(10):5830]. *Med Phys*. 2011;38(7):4296-4311. doi:10.1118/1.3599033
3. Rührnschopf And EP, Klingenbeck K. A general framework and review of scatter correction methods in cone beam CT. Part 2: scatter estimation approaches. *Med Phys*. 2011;38(9):5186-5199. doi:10.1118/1.3589140
4. Maier J, Eulig E, Vöth T, et al. Real-time scatter estimation for medical CT using the deep scatter estimation: method and robustness analysis with respect to different anatomies, dose levels, tube voltages, and data truncation. *Med Phys*. 2019;46(1):238-249. doi:10.1002/mp.13274
5. Chang J, Kim S, Jang D-Y, Suh T-S. A static multi-slit collimator system for scatter reduction in cone-beam CT. *J Appl Clin Med Phys*. 2010;11(4):196-205. doi:10.1120/jacmp.v11i4.3269
6. Stankovic U, Ploeger LS, van Herk M, Sonke JJ. Optimal combination of anti-scatter grids and software correction for CBCT imaging. *Med Phys*. 2017;44(9):4437-4451. doi:10.1002/mp.12385
7. Altunbas C, Kavanagh B, Alexeev T, Miften M. Transmission characteristics of a two dimensional antiscatter grid prototype for CBCT. *Med Phys*. 2017;44(8):3952-3964. doi:10.1002/mp.12346
8. Zhu L, Xie Y, Wang J, Xing L. Scatter correction for cone-beam CT in radiation therapy. *Med Phys*. 2009;36(6):2258-2268. doi:10.1118/1.3130047
9. Roser P, Birkhold A, Preuhs A, et al. X-ray scatter estimation using deep splines. *IEEE Transact Med Imag*. 2021;40(9):2272-2283. doi:10.1109/tmi.2021.3074712
10. Siewerdsen JH, Daly MJ, Bakhtiar B, et al. A simple, direct method for x-ray scatter estimation and correction in digital radiography and cone-beam CT. *Med Phys*. 2006;33(1):187-197. doi:10.1118/1.2148916
11. Jiang Y, Yang C, Yang P, et al. Scatter correction of cone-beam CT using a deep residual convolution neural network (DRCNN). *Phys Med Biol*. 2019;64(14):145003. Published online July 11, 2019. doi:10.1088/1361-6560/ab23a6
12. Cai W, Ning R, Conover D. Scatter correction for clinical cone beam CT breast imaging based on breast phantom studies. *J Xray Sci Technol*. 2011;19(1):91-109. doi:10.3233/XST-2010-0280
13. Li H, Mohan R, Zhu XR. Scatter kernel estimation with an edge-spread function method for cone-beam computed tomography imaging. *Phys Med Biol*. 2008;53(23):6729-6748. doi:10.1088/0031-9155/53/23/006
14. Nomura Y, Xu Q, Shirato H, Shimizu S, Xing L. Projection-domain scatter correction for cone beam computed tomography using a residual convolutional neural network. *Med Phys*. 2019;46(7):3142-3155. doi:10.1002/mp.13583
15. van der Heyden B, Uray M, Fonseca GP, et al. A Monte Carlo based scatter removal method for non-isocentric cone-beam CT acquisitions using a deep convolutional autoencoder. *Phys Med Biol*. 2020;65(14):145002. Published online July 13, 2020. doi:10.1088/1361-6560/ab8954
16. Lee H, Lee J. A deep learning-based scatter correction of simulated x-ray images. *Electronics*. 2019;8(9):944. doi:10.3390/electronics8090944
17. Maspero M, Houweling AC, Savenije MHF, et al. A single neural network for cone-beam computed tomography-based radiotherapy of head-and-neck, lung and breast cancer. *Phys Imaging Radiat Oncol*. 2020;14:24-31. Published online May 25, 2020. doi:10.1016/j.phro.2020.04.002
18. O'Connell A, Conover DL, Zhang Y, et al. Cone-beam CT for breast imaging: radiation dose, breast coverage, and image quality. *AJR Am J Roentgenol*. 2010;195(2):496-509. doi:10.2214/AJR.08.1017
19. Sechopoulos I, Feng SS, D'Orsi CJ. Dosimetric characterization of a dedicated breast computed tomography clinical prototype [published correction appears in *Med Phys*. 2012;39(4):2314]. *Med Phys*. 2010;37(8):4110-4120. doi:10.1118/1.3457331
20. Boone JM, Nelson TR, Lindfors KK, Seibert JA. Dedicated breast CT: radiation dose and image quality evaluation. *Radiology*. 2001;221(3):657-667. doi:10.1148/radiol.2213010334
21. Sarno A, Mettivier G, Russo P. Dedicated breast computed tomography: basic aspects. *Med Phys*. 2015;42(6):2786-2804. doi:10.1118/1.4919441
22. Kwan AL, Boone JM, Shah N. Evaluation of x-ray scatter properties in a dedicated cone-beam breast CT scanner. *Med Phys*. 2005;32(9):2967-2975. doi:10.1118/1.1954908
23. Chen Y, Liu B, O'Connor JM, Didier CS, Glick SJ. Characterization of scatter in cone-beam CT breast imaging: comparison of experimental measurements and Monte Carlo simulation. *Med Phys*. 2009;36(3):857-869. doi:10.1118/1.3077122
24. Kontson K, Jennings RJ. Characterization of scatter magnitude and distribution in dedicated breast computed tomography with bowtie filters. *J Med Imaging (Bellingham)*. 2014;1(3):033505. doi:10.1117/1.JMI.1.3.033505
25. Reiser I, Nishikawa RM, Giger ML, Boone JM, Lindfors KK, Yang K. Automated detection of mass lesions in dedicated breast CT: a preliminary study. *Med Phys*. 2012;39(2):866-873. doi:10.1118/1.3678991
26. Prionas ND, Lindfors KK, Ray S, et al. Contrast-enhanced dedicated breast CT: initial clinical experience. *Radiology*. 2010;256(3):714-723. doi:10.1148/radiol.10092311
27. Prionas ND, Aminololama-Shakeri S, Yang K, Martinez SR, Lindfors KK, Boone JM. Contrast-enhanced dedicated breast CT detection of invasive breast cancer preceding mammographic diagnosis. *Radiol Case Rep*. 2015;10(2):936. doi:10.2484/rcr.v10i2.936
28. Caballo M, Michielsen K, Fedon C, Sechopoulos I. Towards 4D dedicated breast CT perfusion imaging of cancer: development and validation of computer simulated images. *Phys Med Biol*. 2019;64(24):245004. doi:10.1088/1361-6560/ab55ac
29. Ning R, Tang X, Conover D. X-ray scatter correction algorithm for cone beam CT imaging. *Med Phys*. 2004;31(5):1195-1202. doi:10.1118/1.1711475
30. Glick SJ, Didier CS. Can anti-scatter grids improve image quality in breast CT. *IFMBE Proceedings*. 2009:868-870. doi:10.1007/978-3-642-03879-2_243
31. Yang K, Burkett G, Boone JM. A breast-specific, negligible-dose scatter correction technique for dedicated cone-beam breast CT: a physics-based approach to improve Hounsfield Unit accuracy. *Phys Med Biol*. 2014;59(21):6487-6505. doi:10.1088/0031-9155/59/21/6487
32. Sechopoulos I. X-ray scatter correction method for dedicated breast computed tomography. *Med Phys*. 2012;39(5):2896-2903. doi:10.1118/1.4711749
33. Ramamurthy S, D'Orsi CJ, Sechopoulos I. X-ray scatter correction method for dedicated breast computed tomography: improvements and initial patient testing. *Phys Med Biol*. 2016;61(3):1116-1135. doi:10.1088/0031-9155/61/3/1116
34. Ghazi P, Youssefian S, Ghazi T. A novel hardware duo of beam modulation and shielding to reduce scatter acquisition and dose in cone-beam breast CT. *Med Phys*. 2022;49(1):169-185. doi:10.1002/mp.15374
35. Shi L, Vedantham S, Karellas A, Zhu L. Library based x-ray scatter correction for dedicated cone beam breast CT. *Med Phys*. 2016;43(8 Part1):4529-4544. doi:10.1118/1.4955121

36. Shi L, Vedantham S, Karellas A, Zhu L. X-ray scatter correction for dedicated cone beam breast CT using a forward-projection model. *Med Phys*. 2017;44(6):2312-2320. doi:10.1002/mp.12213
37. Caballo M, Boone JM, Mann R, Sechopoulos I. An unsupervised automatic segmentation algorithm for breast tissue classification of dedicated breast computed tomography images. *Med Phys*. 2018;45(6):2542-2559. doi:10.1002/mp.12920
38. Caballo M, Fedon C, Brombal L, Mann R, Longo R, Sechopoulos I. Development of 3D patient-based super-resolution digital breast phantoms using machine learning. *Phys Med Biol*. 2018;63(22):225017. Published online November 12, 2018. doi:10.1088/1361-6560/aae78d
39. Sechopoulos I, Vedantham S, Suryanarayanan S, D'Orsi CJ, Karellas A. Monte Carlo and phantom study of the radiation dose to the body from dedicated CT of the breast. *Radiology*. 2008;247(1):98-105. doi:10.1148/radiol.2471071080
40. Agostinelli S, Allison J, Amako K, et al. Geant4—a simulation toolkit. *Nucl Instrum Methods Phys Res A*. 2003;506(3):250-303. doi:10.1016/s0168-9002(03)01368-8
41. Hernandez AM, Seibert JA, Nosratieh A, Boone JM. Generation and analysis of clinically relevant breast imaging x-ray spectra. *Med Phys*. 2017;44(6):2148-2160. doi:10.1002/mp.12222
42. Sempau J, Sánchez-Reyes A, Salvat F, ben Tahar HO, Jiang SB, Fernández-Varea JM. Monte Carlo simulation of electron beams from an accelerator head using PENELOPE. *Phys Med Biol*. 2001;46(4):1163-1186. doi:10.1088/0031-9155/46/4/318
43. Ronneberger O, Fischer P, Brox T. U-Net: Convolutional networks for biomedical image segmentation. *Lecture Notes Comp Sci*. Published online 2015:234-241. doi:10.1007/978-3-319-24574-4_28
44. Caballo M, Hernandez AM, Lyu SH, et al. Computer-aided diagnosis of masses in breast computed tomography imaging: deep learning model with combined handcrafted and convolutional radiomic features. *J Med Imaging (Bellingham)*. 2021;8(2):024501. doi:10.1117/1.JMI.8.2.024501
45. Hammerstein GR, Miller DW, White DR, Masterson ME, Woodard HQ, Laughlin JS. Absorbed radiation dose in mammography. *Radiology*. 1979;130(2):485-491. doi:10.1148/130.2.485
46. Byng JW, Mainprize JG, Yaffe MJ. X-ray characterization of breast phantom materials [published correction appears in *Phys Med Biol*. 1998;43(10):3161]. *Phys Med Biol*. 1998;43(5):1367-1377. doi:10.1088/0031-9155/43/5/026
47. De Man B, Nuyts J, Dupont P, Marchal G, Suetens P. Reduction of metal streak artifacts in X-ray computed tomography using a transmission maximum a posteriori algorithm. *IEEE Tran Nucl Sci*. 2000;47(3):977-981. doi:10.1109/23.856534
48. Herman G. Correction for beam hardening in computed tomography. *Phys Med Biol*. 1979;24(1):81-106. doi:10.1088/0031-9155/24/1/008
49. Poletti ME, Gonçalves D, Mazzaro I. X-ray scattering from human breast tissues and breast-equivalent materials. *Phys Med Biol*. 2002;47(1):47-63. doi:10.1088/0031-9155/47/1/304
50. Engel KJ, Herrmann C, Zeitler G. X-ray scattering in single- and dual-source CT. *Med Phys*. 2007;35(1):318-332. doi:10.1118/1.2820901
51. Zhu L, Wang J, Xing L. Noise suppression in scatter correction for cone-beam CT. *Med Phys*. 2009;36(3):741-752. doi:10.1118/1.3063001
52. Badal A, Badano A. Accelerating Monte Carlo simulations of photon transport in a voxelized geometry using a massively parallel graphics processing unit. *Med Phys*. 2009;36(11):4878-4880. doi:10.1118/1.3231824
53. Badal A, Sharma D, Graff CG, Zeng R, Badano A. Mammography and breast tomosynthesis simulator for virtual clinical trials. *Comp Phys Comm*. 2021;261:107779. doi:10.1016/j.cpc.2020.107779
54. Gurrola-Ramos J, Dalmau O, Alarcon TE. A residual dense U-net neural network for image denoising. *IEEE Access*. 2021;9:31742-31754. doi:10.1109/access.2021.3061062
55. Huang S-Y, Boone JM, Yang K, et al. The characterization of breast anatomical metrics using dedicated breast CT. *Med Phys*. 2011;38(4):2180-2191. doi:10.1118/1.3567147
56. Yaffe MJ, Boone JM, Packard N, et al. The myth of the 50-50 breast. *Med Phys*. 2009;36(12):5437-5443. doi:10.1118/1.3250863
57. Hernandez AM, Seibert JA, Boone JM. Breast dose in mammography is about 30% lower when realistic heterogeneous glandular distributions are considered. *Med Phys*. 2015;42(11):6337-6348. doi:10.1118/1.4931966

How to cite this article: Pautasso JJ, Caballo M, Mikerov M, Boone JM, Michielsen K, Sechopoulos I. Deep learning for x-ray scatter correction in dedicated breast CT. *Med Phys*. 2023;1-15. https://doi.org/10.1002/mp.16185